Supplement of Solid Earth, 16, 929–945, 2025
https://doi.org/10.5194/se-16-929-2025-supplement

Solid Earth Open Access EGU

Supplement of

Cross-scale strain analysis in the Afar rift (East Africa) from automatic fault mapping and geodesy

Alessandro La Rosa et al.

Correspondence to: Alessandro La Rosa (alessandro.larosa@dst.unipi.it)

Summary of content

The following supplementary material provides additional figures and tables showing details on the fault extraction process and strain calculation, additional tests and ground truth validation of our automatic approach. Figure S1 shows details of the filtering of artifacts, with further details of the normalized scale-dependent linearity filter reported in Table S1. Figures S2 and S3 show the rasterization and the strain calculation processes, respectively. Figures S4 and S5 provide a comparison with results obtained with a 90m DEM, while Figure S6 shows the results of the ground truth validation based on manually mapped faults. Finally, Figure S7 shows the analysis of the distribution of fault dip angles and their effect on the measured strain.

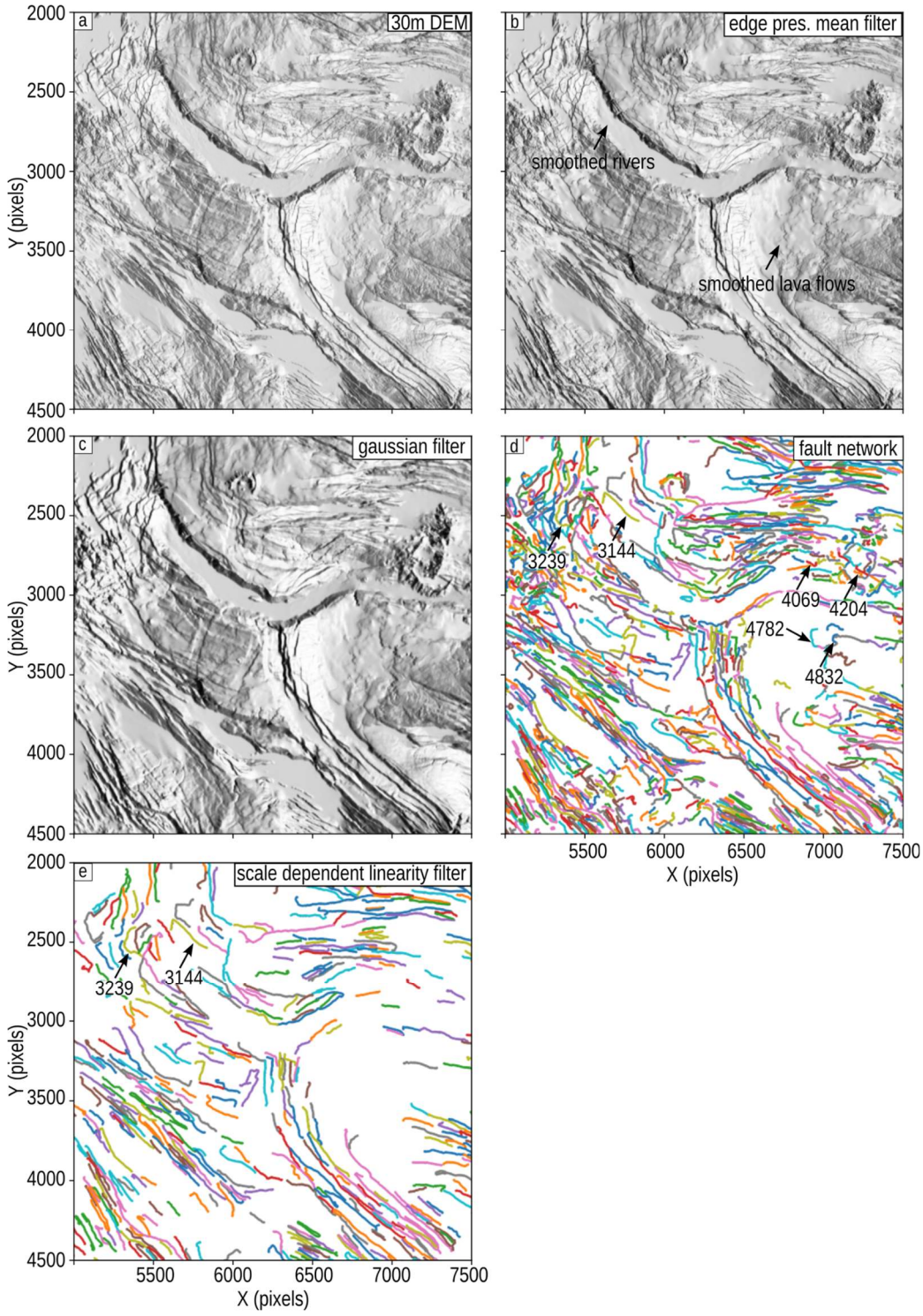

Figure S1 -Filtering method adopted in this study. The area is the same as in Fig.2 a) Original 30 m FABDEM V1-2 DEM (Hawker et al., 2022). b) DEM after the application of the edge preserving mean filter. Note smoothing of undesired morphologies. c) DEM after the application of a low pass Gaussian filter with sigma = 3.5. Note the general smoothing of the surface. d) initial fault network obtained with the Canny edge detection algorithm with minimum/maximum gradient magnitude thresholds of 1/14. The line colors are just representative of fault IDs. The numbers are the IDs of some various detected features including both faults and artifacts. The linearity parameters for these features are reported in Table S1. e) Final fault network after the scale-dependent linearity filter developed in this study. Note that spurious, unrealistically curved segments have been removed by the filter.

ID number	Description	Linearity	Norm. scale-depend. linearity
4782	Curvilinear artifact	0.66	0.32
4832	Curvilinear artifact	0.58	0.11
4204	Small linear artifact	0.79	0.16
4069	Small linear artifact	0.60	0.12
3144	Fault	0.78	1.00
3239	Curvilinear Fault	0.63	0.54

Table S1 – Comparison between linearity and normalized scale-dependent linearity for different features in the network, as shown in Fig. S1. Note that linearity values of both artifacts and faults remain comparable, while the difference between these features increases when calculating the normalized scale-dependent linearity.

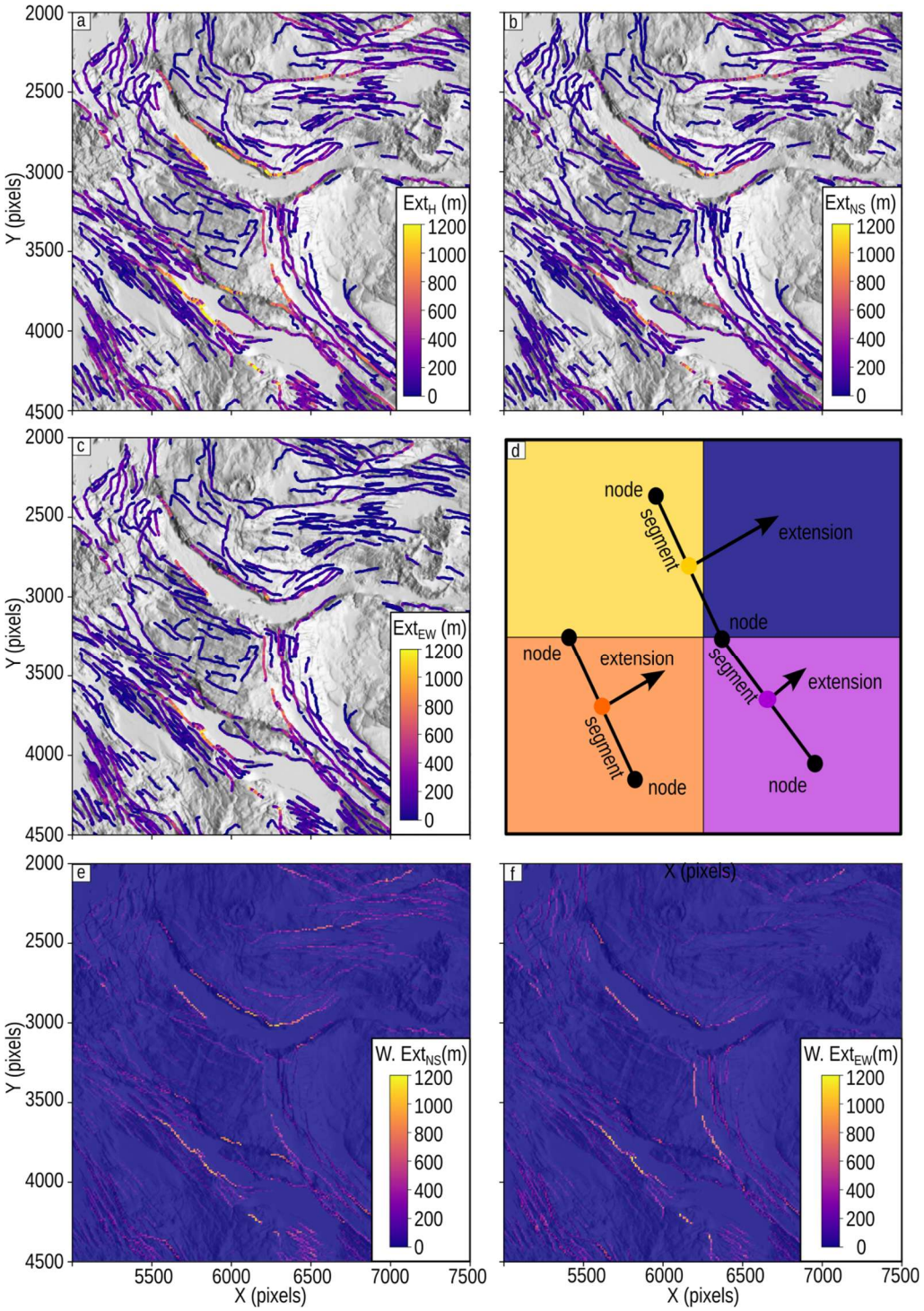

Figure S2 – Workflow steps for the extraction of NS and EW components of extension, and rasterization process. A) Total horizontal extension (Ext_H) measured at each fault segment. b) NS component of extension (Ext_{NS}) measured at each fault segment. c) EW component of extension (Ext_{EW}) measured at each fault segment. d) sketch representing the rasterization process. This method compares spatially the pointwise measurements and a raster of the same area with a given pixel size. If just one measurement falls within the pixel, the latter will assume the corresponding extension values. If more than one pointwise measurement is present within the pixel, the method prevents averaging or summing effects by calculating the length-weighted components of extension ($WExt_{EW}$ and $WExt_{NS}$), corresponding to the sum of products between extension components and fault segment lengths, divided by the total segment length within each pixel. e) Rasterized map of the length-weighted NS component of extension (W. Ext_{NS}). f) Rasterized map of the length-weighted EW component of extension (W. Ext_{EW}). The FABDEM V1-2 DEM (Hawker et al., 2022) is used as figure basis.

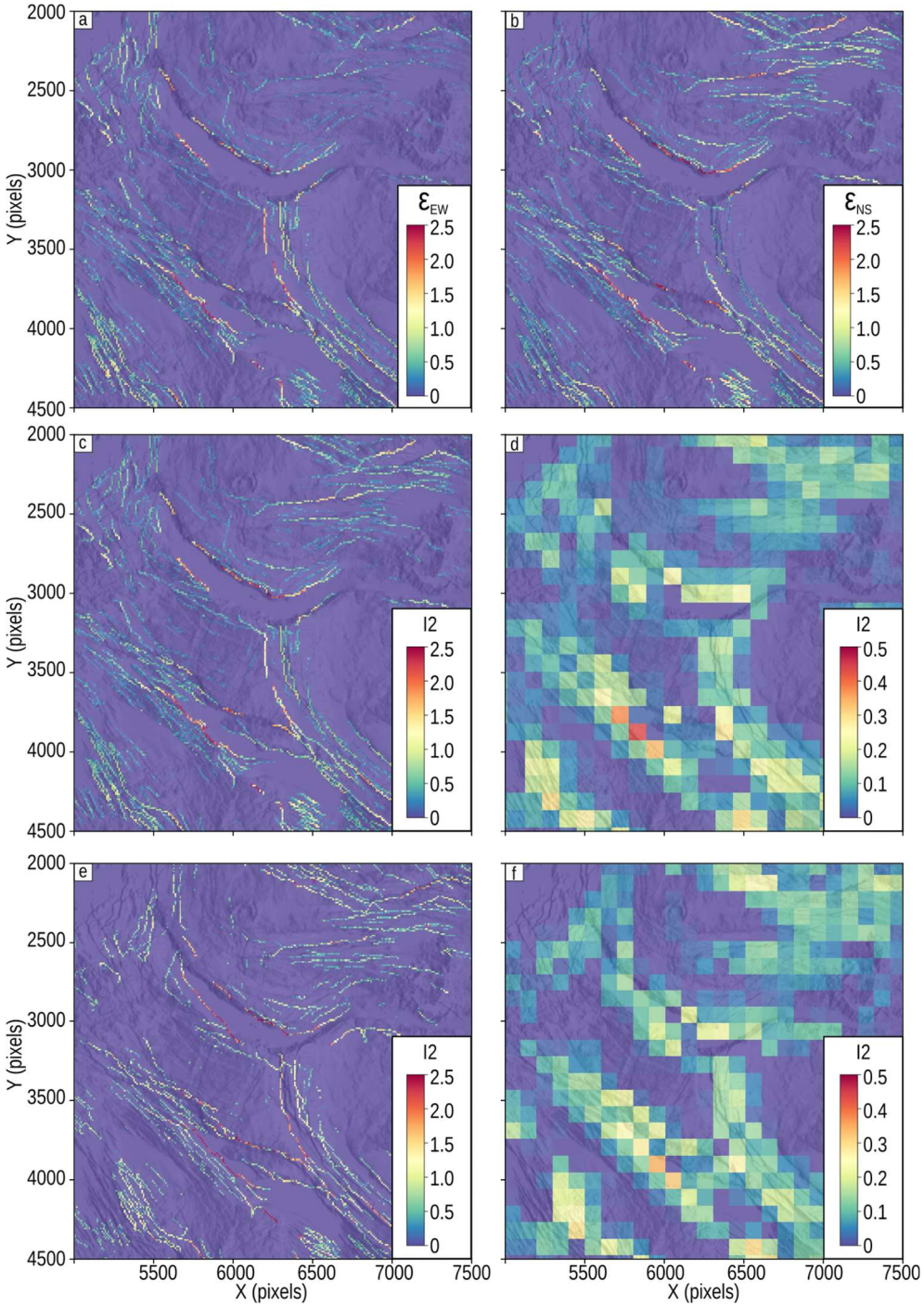

Figure S3 – Calculation and resampling of the geological strain maps, from both 30 m and 90 m Datasets. a) map of the EW component of strain (ε_{EW}) at a resolution of 300 m. b) map of the NS component of strain (ε_{NS}) at a resolution of 0.3 km. c) map of the geological strain magnitude (second invariant, I2) from the 30 m dataset, at resolution of 0.3 km. d) map of the geological strain magnitude (second invariant, I2) from the 30 m dataset, resampled at a resolution of 3 km. e) map of the geological strain magnitude (second invariant, I2) from the 90 m dataset, at resolution of 0.3 km. f) map of the geological strain magnitude (second invariant, I2) from the 90 m dataset, resampled at a resolution of 3 km. The FABDEM V1-2 DEM (Hawker et al., 2022) and the Copernicus GLO 90 m (Airbus, 2020) are used as figure basis.

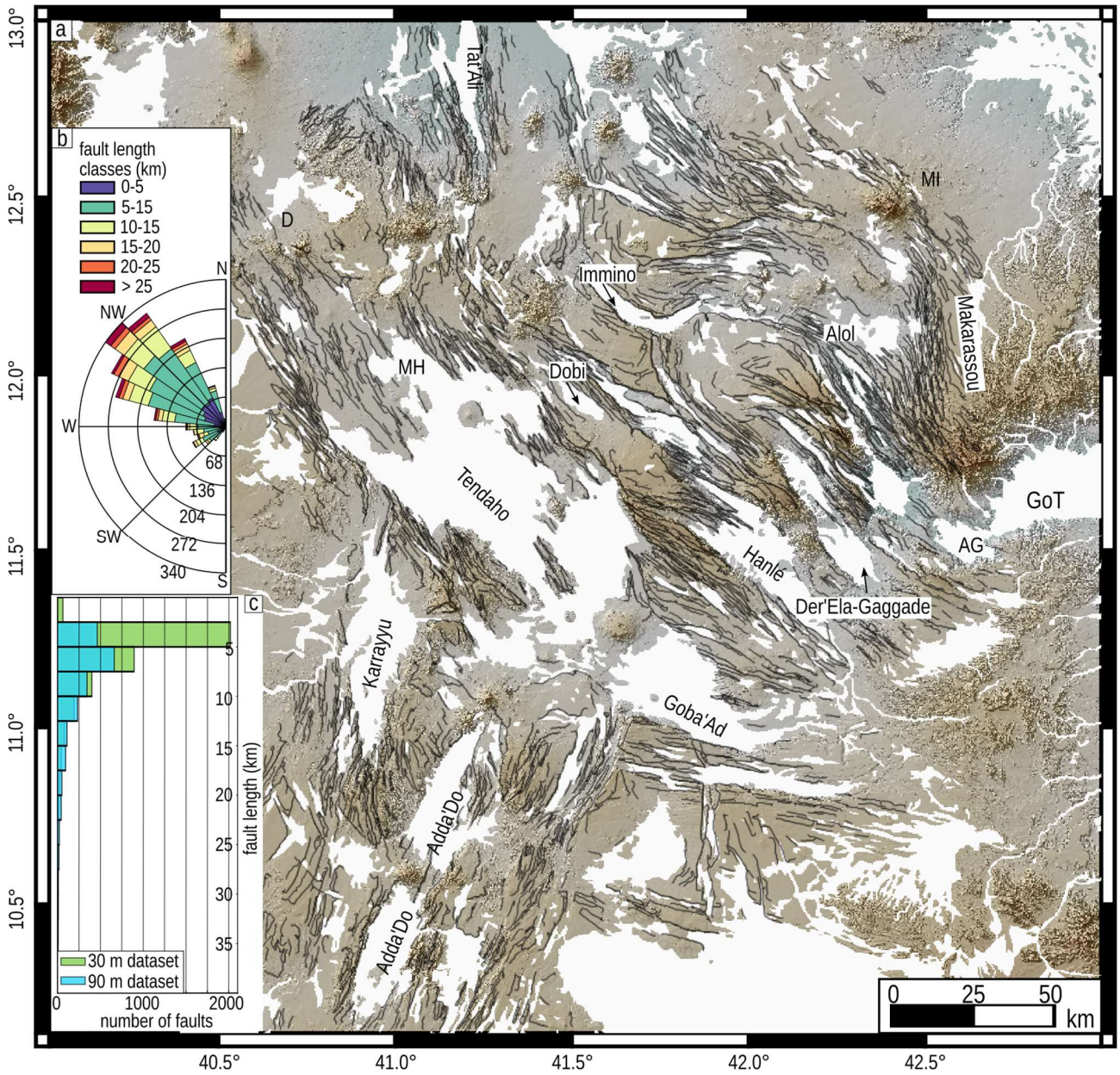

Figure S4 – Results of the automatic fault extraction for the 90 m Dataset and related statistical analysis. a) Map of the faults (black lines) obtained from the 90 m Copernicus DEM (Airbus, 2020). b) length-weighted rose diagrams of fault strike distribution. The rose diagram binning is 10°. c) Histograms comparing the fault-length distributions obtained with a 30 m and a 90 m DEM. The histogram binning is 2.5 km. Names and abbreviations are the same as in Figure 1.

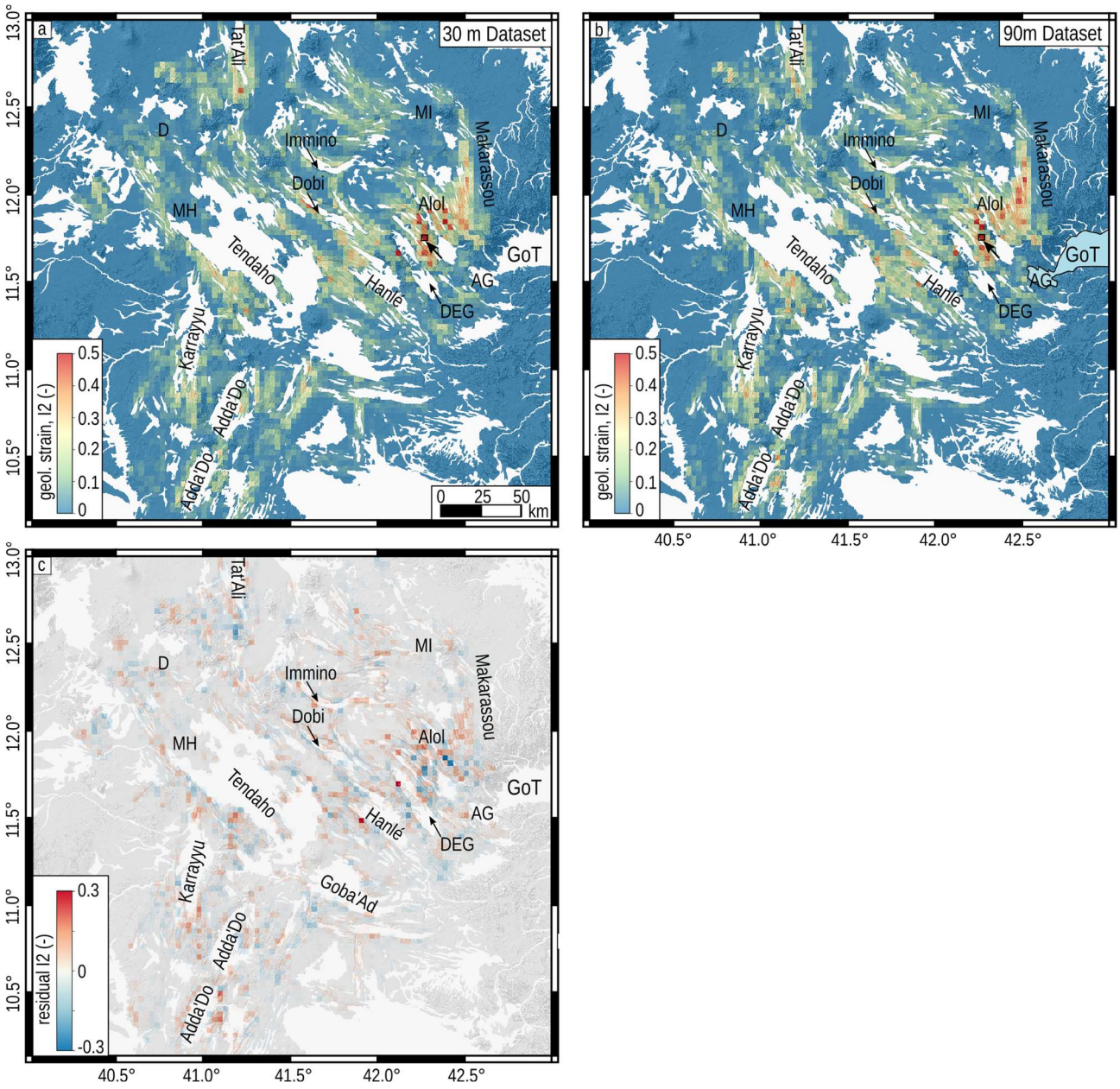

Figure S5 – Maps of geological second invariant of strain I2 for the entire study area. a) I2 from the 30 m dataset. b) I2 from 90 m dataset. Note that we saturated the color bar for values above 0.5 to better highlight the strain variability. The pixel marked by the black rectangle and arrow is an outlier with value of 0.6 associated with an eroded portion of a fault. c) residual between the two maps. First order structures show very good agreement, which means that our workflow provides strain distributions which are independent of the exact resolution of the input DEM. The FABDEM V1-2 DEM (Hawker et al., 2022) and the Copernicus GLO 90 m (Airbus, 2020) are used as figure basis.

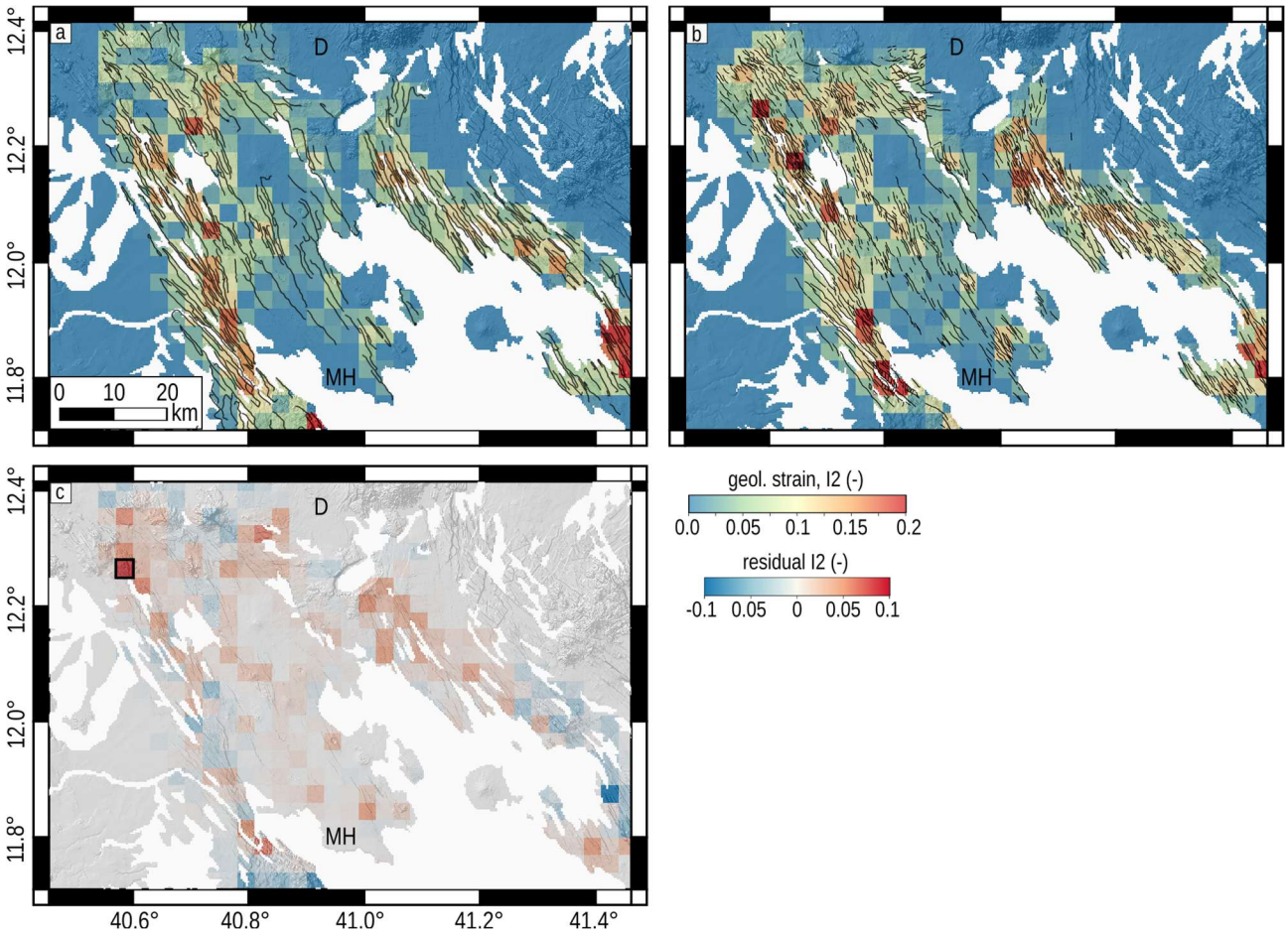

Figure S6 – Results of the ground truth validation. a) Faults and associated geological strain retrieved automatically in the Manda-Harraro segment. b) Faults mapped manually in the same area and associated geological strain. c) Residuals between the two datasets. Black lines are faults. The pixel spacing is 0.3 km. The two datasets show similar strain values and spatial distribution (Fig. S6). Residuals between the manual and automatic datasets range ±0.1, with just an outlier pixel (black rectangle) giving a residual of 0.15. Assuming the manual dataset being representative of 100% of the strain, we calculated that our automatic approach successfully retrieved 93.4% of the total strain. The FABDEM V1-2 DEM (Hawker et al., 2022) is used as figure basis.

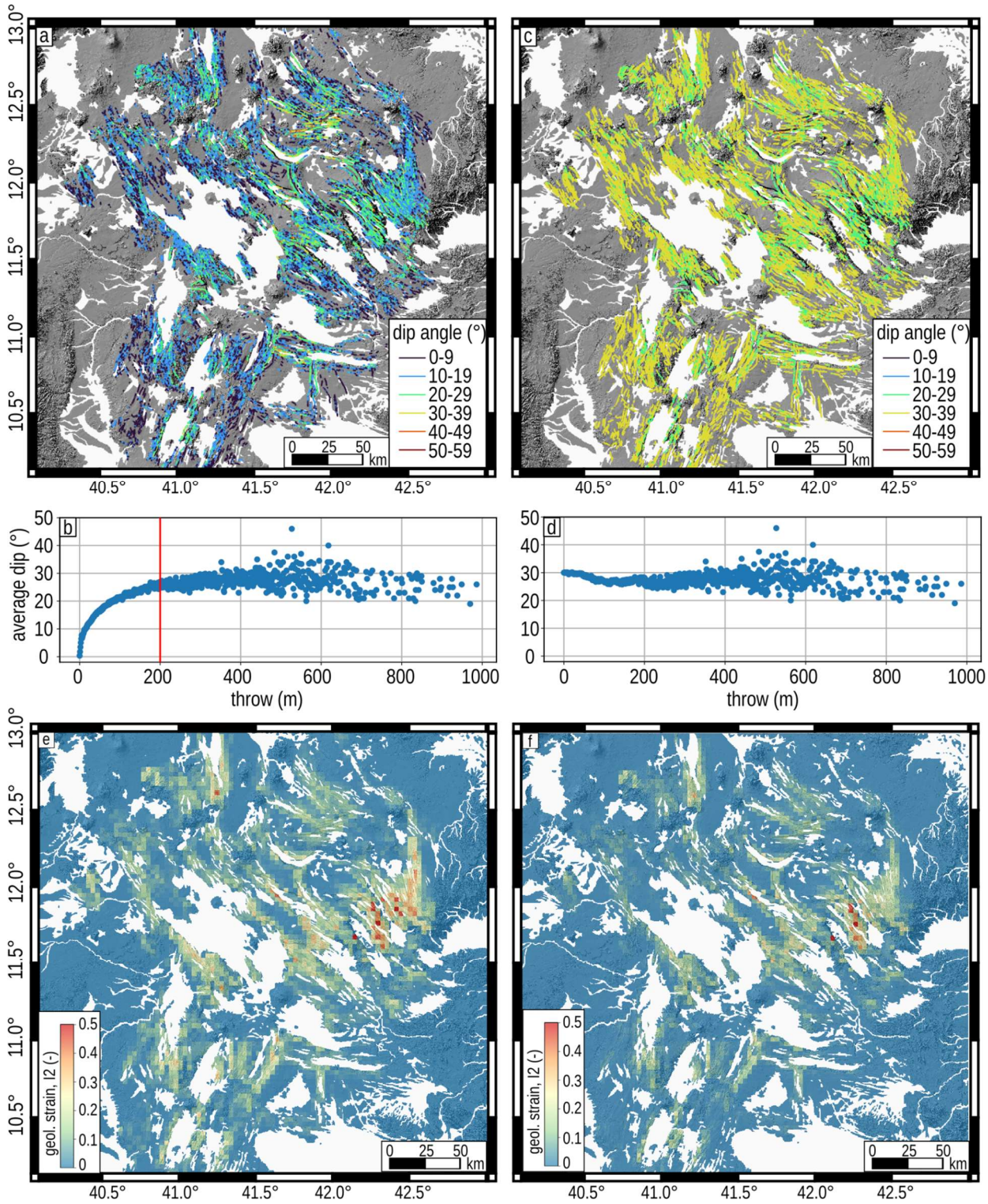

Figure S7 - Analysis of fault dip angles and their influence on geological strains. a) Spatial distribution of dip angles from faults pertaining to the 30m dataset. b) Plot of average fault dip angles as a function of fault throw. For the plot, we rounded throws to the nearest neighbour integer and calculated the average dip angles of fault segments having the same throw in our dataset. The red line marks the throw above which the average dip angle stabilizes around 30°. c) Spatial distribution of recalculated dip angles. We used a fixed dip angle of 30° for faults with throws lower than 200m and dip angle lower than 20°. The plot in d) is similar to that in b) and shows the dip angle correction for faults with throws lower than 200 m. e) Map of geological strain from the 30m dataset, as shown in Fig. S5. f) Strain map from recalculated dip angles. The comparison shows a similar distribution of strain with some decrease mainly observed on minor faults and on the external sectors of the rift. The FABDEM V1-2 DEM (Hawker et al., 2022) is used as figure basis.